



Synthesis of Gold Nanoparticles and Incorporation to a Porous Nickel Electrode to Improve its Catalytic Performance Towards the Hydrogen Evolution Reaction

Ramiro Medina-Orta¹ · Gladis J. Labrada-Delgado² · Héctor G. Silva-Pereyra² · Emma María Ortega³ · Valentín Pérez-Herranz³ · María Guadalupe Sánchez-Loredo⁴

Accepted: 18 September 2021 / Published online: 14 October 2021

© The Author(s), under exclusive licence to Springer Science+Business Media, LLC, part of Springer Nature 2021

Abstract

Gold nanoparticles (AuNPs) were successfully synthesized by a facile chemical reduction method in the presence of the stabilizer polyvinylpyrrolidone and characterized by UV–vis spectroscopy and transmission electron microscopy. The gold nanoparticles were then incorporated onto the surface of a porous Ni electrode by simple addition of the nanoparticles suspension, followed by heat treatment at 350 °C for 1 h under nitrogen atmosphere. The modified electrode was morphologically characterized by field emission scanning electron microscopy. Then, the effect of the modification with Au nanoparticles was studied in the hydrogen evolution reaction (HER) by pseudo-steady-state polarization curves and electrochemical impedance spectroscopy (EIS), at different temperatures and compared with a pure porous Ni electrode. The modified electrode showed a clear improvement in its catalytic performance mainly due to the intrinsic catalytic activity of the Au nanoparticles. From the Tafel representations and the EIS, it was estimated that the HER on the electrode modified with AuNPs takes place by the Volmer-Heyrovsky mechanism.

Keywords Porous Ni electrodes · Au nanoparticles · Chemical synthesis · Hydrogen evolution reaction (HER) · Catalysis

✉ María Guadalupe Sánchez-Loredo
msanchez@uaslp.mx

Ramiro Medina-Orta
ramiro.medina_orta@hotmail.com

Gladis J. Labrada-Delgado
gladis.labrada@ipicyt.edu.mx

Héctor G. Silva-Pereyra
hector.silva@ipicyt.edu.mx

Emma María Ortega
eortega@iqn.upv.es

Valentín Pérez-Herranz
vperez@iqn.upv.es

¹ Universidad Politécnica de San Luis Potosí, Urbano Villalón 500, 78363 San Luis Potosí, México

² Instituto Potosino de Investigación Científica Y Tecnológica, Camino a la Presa San José 2055, 78216 San Luis Potosí, México

³ Departamento de Ingeniería Química Y Nuclear, Universitat Politècnica de València, Camino de Vera s/n, 46022 Valencia, España

⁴ Instituto de Metalurgia/Facultad de Ingeniería, Universidad Autónoma de San Luis Potosí, Sierra Leona 550, 78210 San Luis Potosí, México

Introduction

Metal nanoparticles have received much attention in different fields due to the special properties provided by their high surface-to-volume ratio, in comparison to their bulk counterparts [1–4]. A variety of synthetic approaches have been developed to produce these materials, among them the electrochemical synthesis [5–10] and the chemical reduction methods [11–16]. By both methods, the nanoparticles size and shape depend on a variety of parameters such as the nature and concentration of the precursors, the reducing reagent, and the stabilizing agent [4], being sodium borohydride (NaBH₄) and polyvinylpyrrolidone (PVP) very frequently used as reducing and stabilizing agents, respectively.

Metal nanoparticles have shown an efficient catalytic performance in some reactions [4, 8, 9, 11, 12, 16, 17], including the hydrogen production by alkaline water electrolysis [18–22]. This process is a promising method to produce hydrogen, as a clean and renewable energy carrier. However, it still requires a special effort to reduce the energetic investment for a large-scale production [23–26]. This can be done through the improvement of the intrinsic

catalytic activity of the electrodes or by enlarging their active surface area.

One of the most studied cathode materials for the hydrogen evolution reaction (HER) is metallic nickel, due to its high catalytic activity and low cost [27, 28]. The catalytic performance of Ni can be easily improved by modification with some materials, by means of alloying or co-deposition [29–34]. The addition of metallic nanoparticles results of great interest as it allows the increase of the active surface area of the electrocatalyst by using a small amount of material. Likewise, the nanoparticles could possess strong catalytic activities themselves.

In this work, gold nanoparticles (AuNPs) have been chemically synthesized by a simple chemical reduction method using polyvinylpyrrolidone (PVP) as stabilizer, formation of them was confirmed by UV–vis spectroscopy, and the particles size and morphology were characterized by transmission electron microscopy. The PVP-covered particles were used to modify a nickel microporous electrode in order to improve its catalytic performance in the HER, and for this purpose, they were deposited and heat-treated in a way leading to isolated, well-dispersed nanoparticles. Afterwards, the morphology of the nanoparticles after the heat treatment and the structure of the deposits were observed by means of field emission scanning electron microscopy (FESEM). The chemical composition of the modified electrode and the gold presence were confirmed by energy-dispersive X-ray spectroscopy (EDS). Finally, the electrodes were electrochemically assessed and compared by Tafel pseudo-steady-state polarization curves and electrochemical impedance spectroscopy (EIS), at different temperatures. Gold is considered by researchers as a less efficient HER catalyst, when compared to Pt, because the adsorption strength of hydrogen atoms on gold surfaces is weaker; nevertheless, some authors have found that Au nanoparticles are able to synergistically enhance the activity of non-metallic HER catalysts [35–38].

Experimental

Synthesis and Characterization of Au Nanoparticles

The synthesis of Au nanoparticles was based on the chemical reduction in aqueous media from a solution containing 0.05 M sodium tetrachloroaurate(III) (SIGMA-ALDRICH) and 20 g L⁻¹ polyvinylpyrrolidone (PVP, MW 40,000 g mol⁻¹) (SIGMA-ALDRICH) as stabilizing agent, in deionized water. The reduction process was performed by rapid addition of a 0.0125 M sodium borohydride solution, containing 20 g L⁻¹ PVP and 0.1 M

sodium hydroxide, under sonication. The volume ratio was 1:1. The as-prepared nanoparticles were optically characterized using an UV/VIS spectrometer Lambda 35 (Perkin Elmer Inc.) in absorbance mode, in the range of 200–800 nm, and morphologically by means of a FEI TECNAI F30 FEG-transmission electron microscope (300 kV) in scanning mode (STEM) with a HAADF detector (Z-contrast).

Modification of the Porous Nickel Electrode

A porous nickel electrode (0.5 cm² geometric area) was used as the base electrode for the modification with AuNPs. This electrode was fabricated by electrodeposition at a high current density on a stainless steel AISI 304 substrate, as reported in previous works [34, 39]. The modification was carried out by diluting 500 µL of the AuNPs dispersion in 3 mL of deionized water and dropping 40 µL of the resulting dilution onto the electrode's surface. Then, the electrode was subjected to heat treatment at 350 °C for 1 h under a nitrogen atmosphere, and images using both backscattering and secondary electron detectors were obtained using field emission scanning electron microscopy (FESEM) with a FIB DUALBEAM FEI HELIOS 600 NANOLAB scanning electron microscope (the Netherlands), located at the IPICYT (San Luis Potosí). The modified electrodes before and after the electrochemical characterization were also observed with a FEI QUANTA 250 scanning electron microscope.

Electrochemical Characterization

The influence of the AuNPs on the hydrogen evolution reaction was assessed by means of Tafel representations obtained from pseudo-steady-state polarization curves and electrochemical impedance spectroscopy (EIS). The electrochemical characterization was carried out using a Potentiostat Galvanostat PAR Ametek, model VersaStat 3F. These procedures were carried out in an oxygen free 30 wt% KOH solution, prepared by bubbling with N₂ for 15 min. The polarization curves were recorded from -1.4 V vs SHE to the equilibrium potential at a scan rate of 1 mV/s. Before the tests, the working electrode was held at -1.45 V in the same solution, in order to reduce the oxide film existing on the porous surface electrode layer, for 30 min to establish reproducible polarization diagrams.

After the polarization curves, EIS measurements were recorded at four different overpotentials from 0 to 150 mV in a frequency range from 10 kHz to 5 mHz at 10 frequencies per decade applying a sinusoidal signal of 10 mV peak-to-peak. The impedance response was fitted by an equivalent circuit using the complex non-linear least square (CNLS) method with the ZView 3.0 software. All these experiments were

performed at 40, 60, and 80 °C. The real and imaginary parts of the EIS were normalized with respect to the geometric surface of the electrodes.

Results and Discussion

Synthesis and Characterization of Au Nanoparticles

In order to reduce the aggregation of the nanoparticles during the synthesis, PVP was added to both precursor solutions, expecting the polymer could act as an efficient coating agent for the growing gold nanoparticles, to enhance the stability of the nanoparticle concentrated colloid, and hoping it would contribute to avoid agglomeration of the particles during the electrode modification, by steric effects. After the synthesis, the dispersion containing AuNPs was optically followed for several days by UV–vis spectroscopy in a wavelength range from 300 to 800 nm. Figure 1 shows the UV–vis spectra of the AuNPs the first three days after the preparation. A clear surface plasmon can be observed at 544 nm after the synthesis, which agrees with other UV–vis spectra for gold colloids found in the literature [17, 18, 40]. However, the reaction and growth process continued until certain stabilization is reached, as observed in the spectra of the next 2 days, where the surface plasmons show a slight blueshift (536 nm) and an increase in the absorbance, the latter probably because the existent gold clusters, composed of only few atoms, start to form more nanoparticles. The dependence of the UV/vis absorption maximum on the size

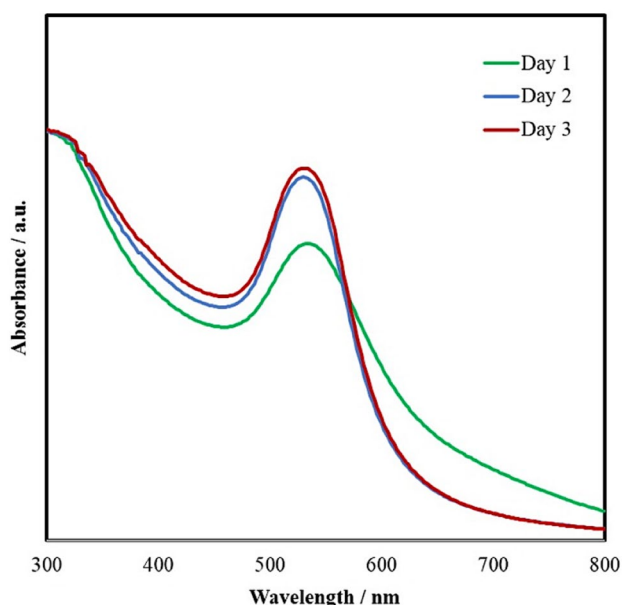


Fig. 1 UV–vis spectra of AuNPs dispersion during the first 3 days from the synthesis

of metal spherical particles was already reported, where the absorption peak shifts towards longer wavelengths as particles become bigger [41]. In this case, the formation of new and smaller particles may lead to a shift to shorter wavelengths as the mean size of the particles is different to that at the first day of the synthesis. The suspensions were stable even for several months after preparation.

The TEM micrographs of the AuNPs are displayed in Fig. 2. A size distribution was observed ranging from single nanoparticles of 5 to 45 nm with an irregular, potato-like morphology (Fig. 2a and 2d). Figure 2b and 2e show the particles from Fig. 2a and 2d, where the PVP coverage is evident. Figure 2c shows the histogram of the synthesized gold nanoparticles and Fig. 2f the PVP shell width. The stabilizing power of the polymer PVP is clearly appreciated, as the TEM images capture the polymer shells, not uniform, surrounding the AuNPs. PVP, a bulky, non-toxic, and non-ionic polymeric reducing agent, acts as an effective surface stabilizer, growth modifier, and nanoparticle dispersant, depending its role on the kind of synthesis and the parameters used [42]. PVP possess multiple >C=O and C–N groups, included in a strong hydrophilic part (the pyrrolidone moiety, the head group), and CH₂ groups (the polyvinyl backbone, the hydrophobic part tuning the distances among adsorbed head groups). The polymer acts preventing aggregation of the colloids, where the repulsive forces arise from the hydrophobic chains that extend into the solvent, interacting with each other (steric hindrance effect) [43]. Both the >N– and >C=O groups are able to anchor to the particles surface via coordinative interactions. Some authors reported that PVP binds to Ag nanoparticles using the highly polar carbonyl group, where the polymer donates a lone electron pair from the donor atom to the orbital of the ionic Ag; others propose that the coordination of the polymer to the metal depends on the size of the particles [44–46].

In the case of submicron-sized colloids, it was stated that the coordination of the PVP to the metal takes place through the nitrogen-containing heterocyclic ring of the PVP, whereas the carbonyl group binds more strongly to nanometrical particles [47]. According to some authors, when dissolved, the polymer PVP adopts a pseudo-random coil structure with spherical shape [48, 49], and after dissolving the metal precursor in the PVP solution, the metallic species are adsorbed on the surface of the polymeric random coils, and they slowly diffuse towards the sphere's center. The borohydride ions, also located inside the polymeric structure, should then lead to the reduction of the metal ions. As both diffusion and reduction take time to occur, the authors state that the presence of metal atoms neighboring the random coil surface is more important than in the center, so that the nucleation starts at the point of the random coil surface, where supersaturation is higher. Phase separation and clusters growth then should take place

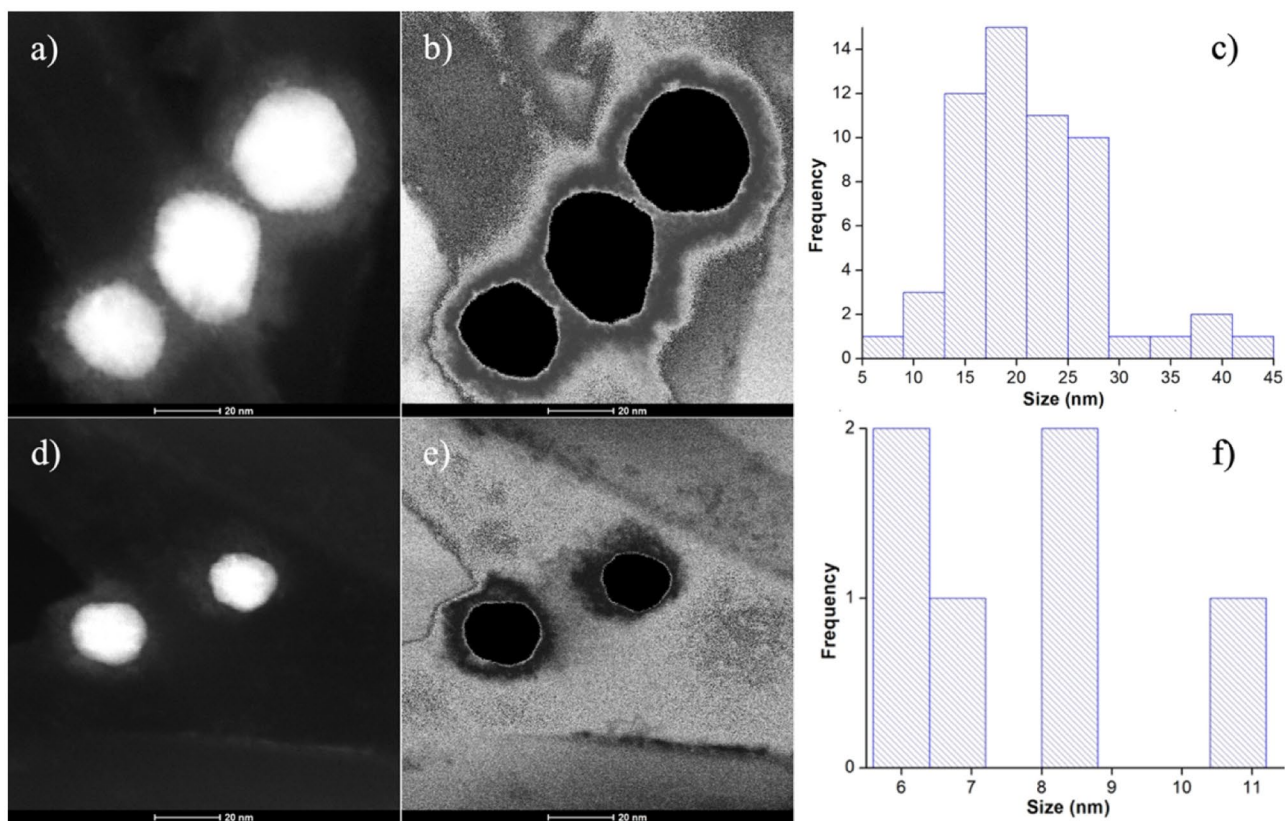


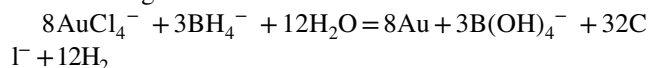
Fig. 2 TEM micrographs of AuNPs showing (a) and (d) irregular potato-like nanoparticles showing the presence of PVP on the surface; (b) and (e) irregular nanoparticles showing the core-shell struc-

ture promoted by the PVP on the surface, (c) size distributions of irregular potato-like AuNPs, and (f) PVP shell width

by absorption of the metallic atoms from the surroundings, lowering the local concentration of metal atoms. That means, once the cluster is produced, it could act as diffusion center. The clusters grow by diffusion-deposition of the metallic atoms. At higher PVP concentrations, with the polymer adsorbed at full coverage, the saturation coverage of the particles is larger than the monolayer coverage, and therefore, the adsorbed polymer is not lying close to the surface, but extends away from the surface like a carpet of loops and tails [50].

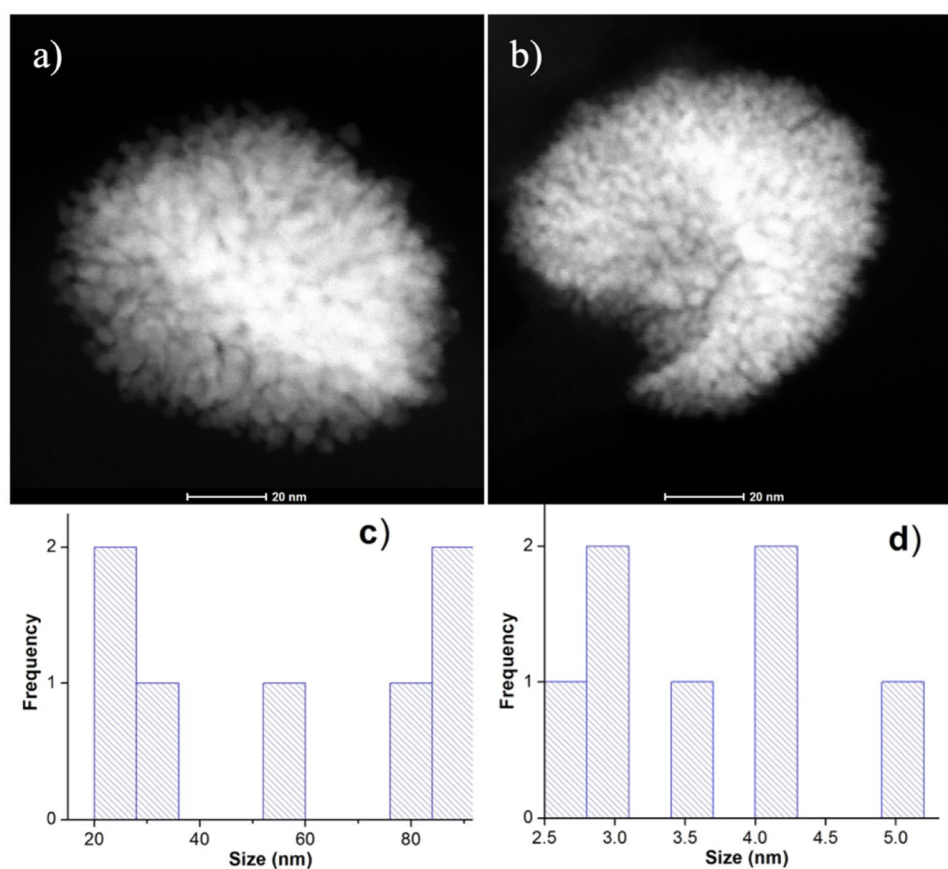
Particularly interesting is the presence of few particles looking like nanoshrimps and nanoflowers (Fig. 3a and 3b); they are present in very small amounts in the sample; nevertheless, they possess a significant surface area. Dimensions of the nanoshrimps and nanoflowers are ~80 nm (bud size), and the single crystalline petal thickness varied from ~2.5 to 5 nm (Fig. 3c), with rough surfaces. They are unique nanostructures, self-assemblies of smaller particles, as a result of an aggregation mechanism. Due to the coarse surfaces and high surface-to-volume ratios, reported 3D hierarchical gold nanoflowers have shown outstanding performances in cell imaging, catalysis, surface-enhanced Raman scattering, and photothermal conversion [51]. In general, the borohydride

ions act as reducing agent for the AuCl_4^- ions according to the following reaction:



BH_4^- is not only an efficient reducing agent, but at low or moderate PVP concentrations, it is expected that the excess borohydride ions could participate in the capping activity, competing with the PVP chains. In the synthesis used in this work, the BH_4^- concentration is lower than the PVP concentration but higher than the stoichiometric AuCl_4^- concentration. Therefore, it cannot be ruled out that, after formation, the nuclei could possibly be surrounded first by the excess BH_4^- ions, as they are small and diffuse faster than the bulkier PVP molecule. Tang et al. [45] propose that, for this reason, surface instability of the forming particles takes place, resulting from the partial desorption of capping reagents. In this work, this desorption of the small BH_4^- ions would expose bare Au surfaces, leading to a stacking growth of Au atoms on the particles' surfaces, or to possible diffusion and fusion of the smaller primary particles, and finally, to formation of the nanoshrimps and nanoflowers by aggregation mechanism.

Fig. 3 (a) Nanoflower, (b) nanoshrimp made by smaller AuNPs, and size distribution of (c) nanoshrimps and nanoflowers; (d) petals of the nanoflowers



Once synthesized and characterized, the AuNPs were used to modify the surface of a porous Ni electrode by a heat treatment at 350 °C under N₂ atmosphere for 1 h. The nanoparticles were incorporated on the nickel surface, under oxygen-free conditions, using a 1:6 dilution of the as-prepared nanoparticles dispersion. Free PVP decomposes around 400 °C in air [50]. When bound to Ag nanoparticles, PVP decomposition temperatures between 200 and 400 °C have been reported for different experimental conditions. That means, it is highly probable that the PVP decomposes when the modified electrode is heat-treated.

The micrographs in Fig. 4 show the microstructure of the electrode (right side) at three different magnifications. The left side shows high-resolution FESEM images taken using the backscattered electrons detector, useful for obtaining information about size, size distribution, and aggregation degree of the AuNPs on the electrode. From the image at high magnifications, the adequate dispersion and low aggregation degree of the Au nanoparticles are evident, demonstrating the good capping ability of the polymeric stabilizer PVP.

The histogram of the AuNPs measuring 381 particles is shown in Fig. 5. The figure shows that the heat treatment does not affect the final particles size, where most of the particles are in the range of 7 to 14 nm. The energy dispersive

X-ray analysis (EDS) spectrum of Fig. 6 confirms the presence of the AuNPs on the electrode's surface.

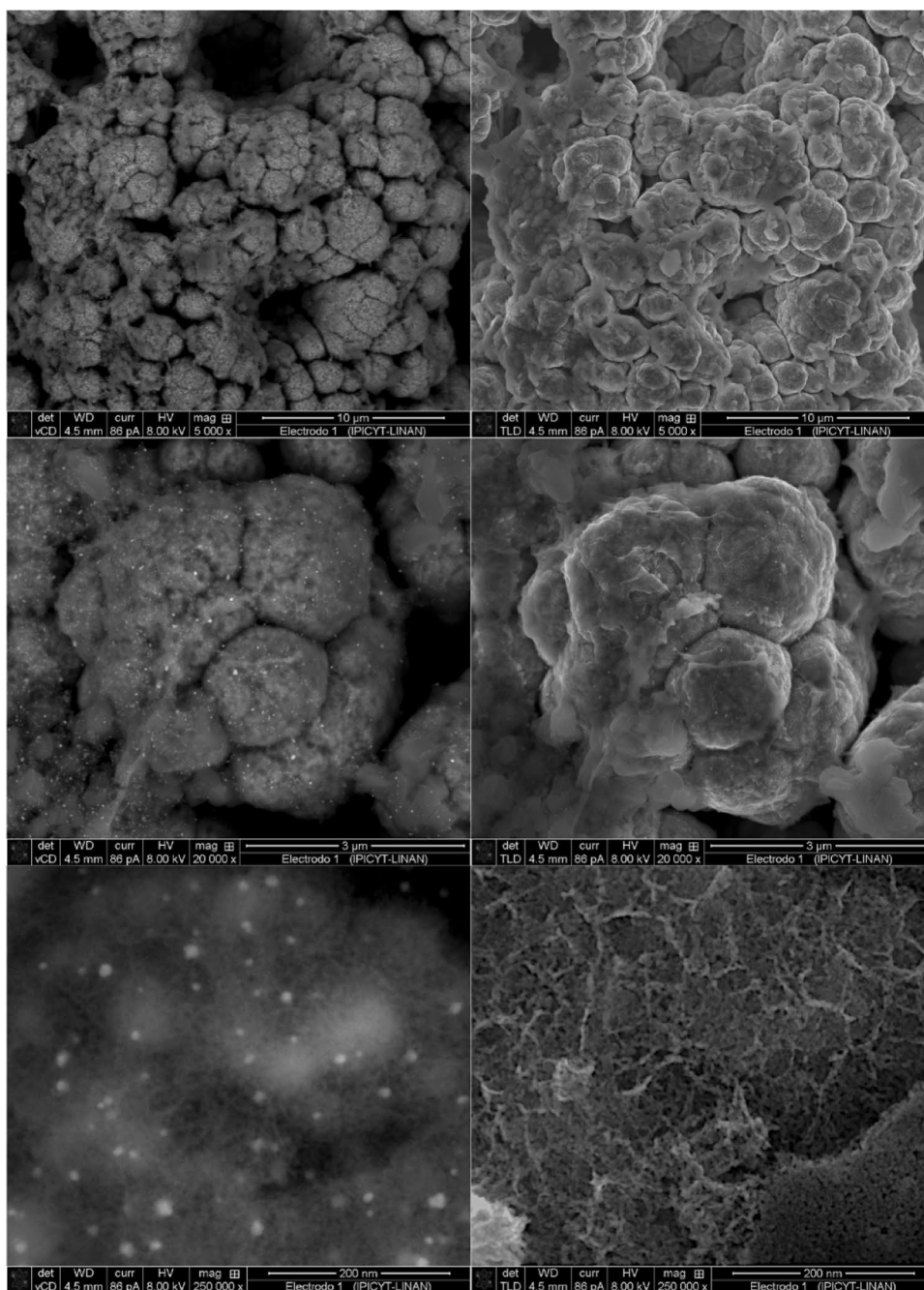
The heat treatment seems adequate to fix the AuNPs to the electrode, as the nanoparticles remain adhered to the surface after the electrochemical measurements (Fig. S1, ESI file), the presence of the PVP coverage during the heat treatment helps prevent the agglomeration as a result of steric effects. Also, the electrodes show no change due to the presence of impurities from the electrolysis procedure.

Electrochemical Measurements

The potential catalytic effect of the AuNPs on the porous Ni electrode in the HER was assessed by Tafel representations obtained from pseudo-steady-state polarization curves. The Tafel representations of the electrode modified with AuNPs at 40, 60, and 80 °C in 30 wt% KOH are compared in Fig. S2 (ESI file) with the representations of the non-modified porous Ni electrode. These curves were corrected from de pseudo-steady-state polarization curves with respect to the equilibrium potential and the ohmic drop as:

$$\eta = E - E_{eq} - j \cdot R_s \quad (1)$$

Fig. 4 FESEM micrographs of the porous Ni electrode modified with AuNPs. (Left side) images at three different magnifications showing the AuNPs on the surface of the electrode (backscattered electrons detector), and (right side) structure of the electrodes at different magnifications (secondary electrons detector)



were η is the overpotential, E_{eq} is the equilibrium potential determined from the semilogarithmic plot of E vs $\log|j|$, and R_s ($\Omega \text{ cm}^2$) is the electrolyte resistance between the working electrode and the reference electrode and was calculated as the intersection of the impedance spectra at high frequencies (or its prolongation) with the x -axis in the complex plane.

The linear behavior at high overpotentials can be described by the Tafel equation:

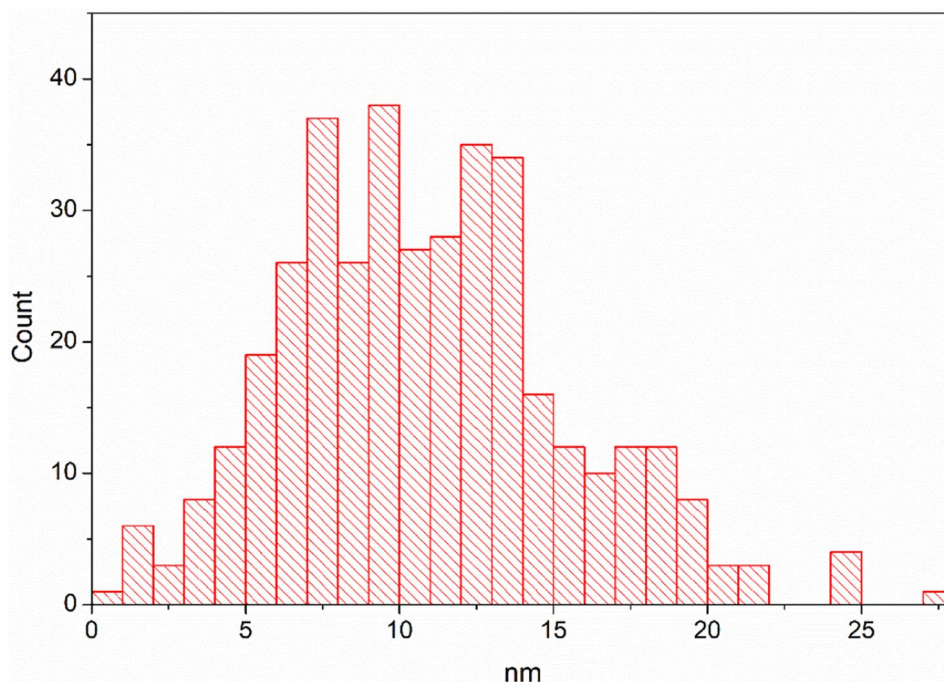
$$\eta = a + b \cdot \log j \quad (2)$$

where b is the Tafel slope, j is the current density, and a is the intercept, and it is related to the exchange current density as in the Eq. (3):

$$a = \frac{2.3RT}{\alpha F} \log j_0 \quad (3)$$

where R is the gas constant, T is the temperature in K, F is de Faraday constant, and α is the charge transfer coefficient, which is related to the Tafel slope by the Eq. (4):

Fig. 5 Size distribution of AuNPs deposited on the modified Ni electrode after heat treatment at 350 °C under nitrogen atmosphere



$$b = -\frac{2.3RT}{\alpha F} \quad (4)$$

The kinetic parameters shown in the Eqs. (2), (3), and (4) can be determined from the linear region of the Tafel representations. These parameters are reported in Table S1 (ESI) with η_{100} , which represents the overpotential required to reach a current density of 100 mA cm⁻², related to the energy necessary to produce a determined amount of hydrogen, a useful parameter in the comparison of the catalytic activity of the electrodes [22, 32–34, 39, 52].

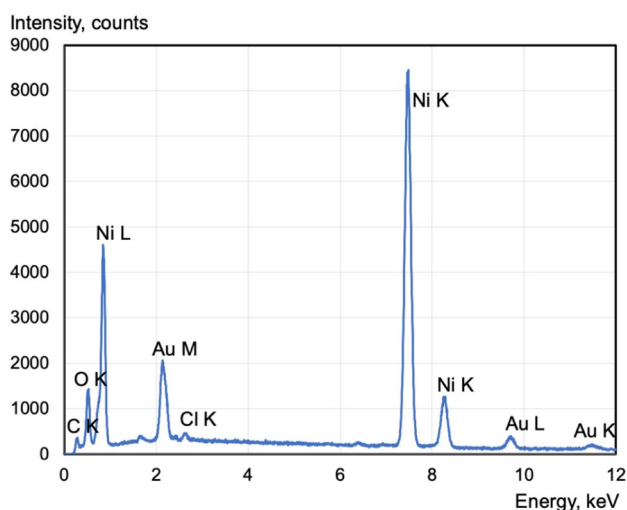


Fig. 6 Energy dispersive X-ray spectrum of the modified electrode surface

The porous Ni electrode shows Tafel slopes and charge transfer coefficients like those reported in the literature for a Volmer-Heyrovsky mechanism in the HER [27, 53], whereas the electrode modified with AuNPs (Ni-AuNPs) shows an important increase in b and a decrease in α . This can be explained by the increase in the active surface area provided by the AuNPs, since these values do not correspond to the other mechanisms for the HER [27, 53–56]. Since the catalytic activity towards the HER depends on both j_0 and b , for sufficiently high overpotentials, the effect of the high Tafel slope prevails over j_0 , and the HER activity will be higher for the porous Ni electrode. However, in the range of current densities used in this work, and particularly in the range between 100 and 600 mA cm⁻², typical of industrial electrolyzers, the activity of Ni-AuNPs electrode is higher than for the porous Ni electrode.

On the other hand, it can be observed that the exchange current density values are higher for Ni-AuNPs, whereas η_{100} values are substantially lower. This is related to an increase in the catalytic activity of the electrode [34, 39, 57]. Also, for both electrodes, the catalytic activity increases with temperature.

Another parameter related to the catalytic activity is the apparent activation energy (E_a). It can be related to the

Table 1 Activation energies of the electrocatalysts obtained in 30 wt% KOH

Electrocatalyst	E_a (kJ mol ⁻¹)
Porous Ni	48.0 ± 0.5
Ni-AuNPs	38.0 ± 0.3

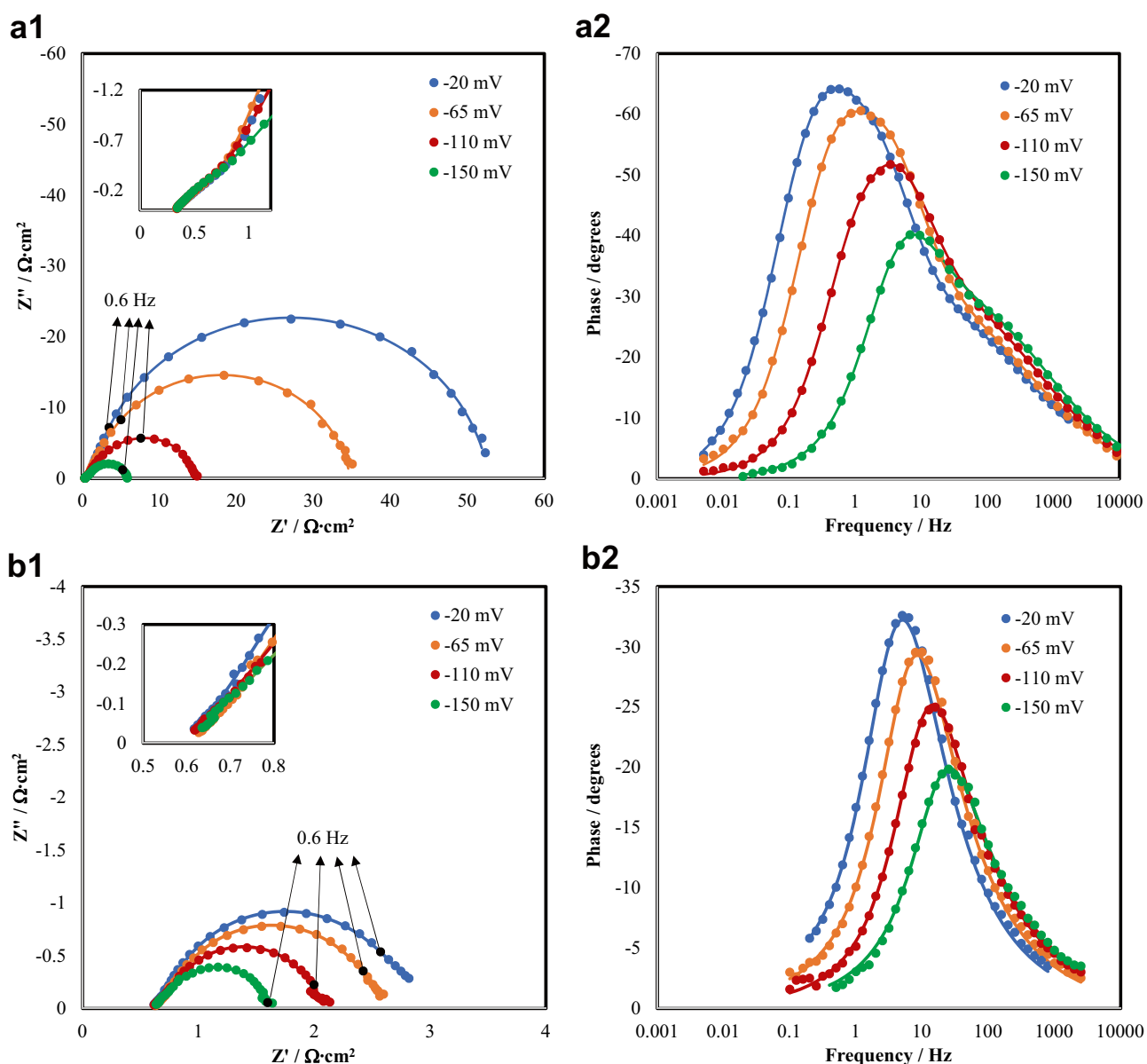


Fig. 7 EIS representations of the investigated electrocatalysts obtained in 30 wt% KOH at 40 °C: **a1** (porous Ni), **b1** (Ni-AuNPs), Nyquist representations, **a2** (porous Ni), **b2** (Ni-AuNPs), Bode representations of the phase angle as a function of frequency

exchange current density and is calculated from an Arrhenius representation (Eq. (5)):

$$\log j_0 = A' - \frac{E_a}{2.303R} \cdot \frac{1}{T} \quad (5)$$

The representations of both electrodes are shown in Fig. S3 (ESI), with the corresponding Arrhenius expressions. The values of E_a are reported in Table 1 for both electrodes.

Generally, the E_a at the equilibrium potential ($\eta = 0$) for any electrode reaction is considered as a feature of electrocatalysis when it is evaluated at various electrode materials

in the same electrolyte. On this basis, the obtained values for E_a shown in Table 1 are in the same order of magnitude than that reported for other authors on Ni catalysts, which ranged from 38 to 60 kJ mol⁻¹ for different Ni-Co electrodes [34]. On Pt/Ni electrodes, an apparent activation energy of 56 kJ mol⁻¹ was obtained by Correia and Machado [58], while Savadogo and Ndzebet [59] obtained a value of 45 kJ mol⁻¹ on Pt-Co alloy supported on carbon. On the other hand, González-Buch et al. found a value of 51.9 kJ mol⁻¹ for the E_a obtained for Au-modified microporous Ni electrodes [19]. The values found for the free activation energy are very close to those usually postulated for the

HER occurring through the Volmer-Heyrovsky mechanism on Ni surfaces [60, 61].

From these results, it can be concluded that the addition of AuNPs improves the catalytic activity of the electrode, since a lower activation energy represents a lower energy requirement for the hydrogen production. This improvement in the catalytic activity of the electrodes can be due to the increase of the active surface area or by the effect of the intrinsic catalytic activity of the additional material [57]. In order to determine which of these reasons is responsible for the improvement of the catalytic activity of the electrode, the effective surface area must be calculated. This can be done through EIS measurements. The EIS spectra of both electrodes collected at different overpotential values selected from Fig. S2 (ESI) are shown in Fig. 7.

Figure 7a1 and 7b1 show the Nyquist representations of the porous Ni electrode and Ni-AuNPs, respectively, at 40 °C and different overpotentials. It can be observed for both electrodes that the total resistance decreases with the overpotential. The Nyquist representation of the porous Ni electrode is characterized by two superimposed semicircles (that is, two-time constants) [34, 39, 52, 62], in the middle to low frequencies range, which can also be observed in the Bode representation of the phase angle as a function of frequency (Fig. 7a2). On the other hand, for Ni-AuNPs, there is only one semicircle in the Nyquist representation, which is clear by the sharp maximum observed in the Bode representation (Fig. 7b2). For both electrodes, as shown in the insets in Fig. 7a1 and 7b1, at high frequencies, a small semicircle, independent of both temperature and overpotential, which is related to the porosity is observed [62, 63].

In order to describe the impedance data, several models were tested, and the appropriate model was selected. First of all, the Levie's finite length porous model [64] was rejected as it did not produce a good fit at high frequencies. Then, the experimental impedance data were fitted to the models

presented in Fig. 8. The 2CPE serial model (Fig. 8A) introduced by Chen and Lasia [65] produces two semicircles: the first one, potential independent, is related to the surface porosity, and the second, potential dependent, is related to the HER. This model was used to fit the impedance data obtained with the Ni-AuNPs electrode. For the porous Ni electrode, in which two semicircles dependent on both overpotential and temperature were obtained in the middle to low frequencies range and a small semicircle independent of overpotential at high frequencies, the EIS spectra were modeled by using the two-time constant parallel equivalent circuit proposed by Armstrong and Henderson [66] in series with a CPE (CPE₁ in Fig. 8B). In this model, CPE₁ is related to the electrode porosity, and the other two-time constants are related to the charge transfer kinetics and to the hydrogen adsorption [31, 62].

Figure 7 shows that the EEC used properly models for the alternating current response of the investigated materials, manifesting an excellent agreement between the experimental (symbols) and CNLS fitting (lines) data. Table 2 reports the EEC parameters values obtained from the experimental impedance data fitting on the investigated electrodes at 40 and 80 °C. The values of C_{dl} for both electrodes were calculated using the equation proposed by Brug et al. [67] modified as:

$$C_{dl} = Q_2^{1/n_2} \left[\frac{1}{R_s + R_1} + \frac{1}{R_2} \right]^{1-\frac{1}{n_2}} \quad (6)$$

where Q_2 is the CPE constant and n_2 is the CPE exponent, R_s is the solution resistance, R_1 is the resistance associated to the electrode porosity, and R_2 is the charge transfer resistance.

According to the circuit values collected in Table 2, for the porous Ni electrode, the high-frequency semicircle is almost constant with the overpotential and is related to the

Fig. 8 Equivalent circuit models used to adjust the impedance response of the developed electrocatalysts: (A) 2CPE serial model for Ni-AuNPs, (B) two-time constant parallel model with a serial CPE for porous Ni

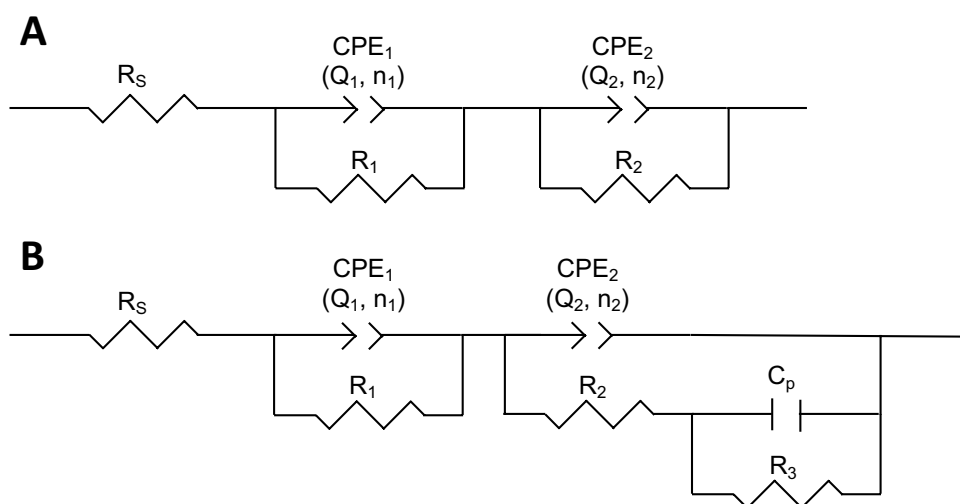


Table 2 Parameters determined by fitting EIS experimental spectra in 30 wt% KOH

Temperature	40 °C				80 °C			
Porous Ni								
η (mV)	–20 mV	–65 mV	–110 mV	–150 mV	–20 mV	–65 mV	–110 mV	–150 mV
R_s ($\Omega \text{ cm}^2$)	0.32 ± 0.07	0.32 ± 0.07	0.32 ± 0.08	0.32 ± 0.07	0.22 ± 0.04	0.22 ± 0.05	0.22 ± 0.04	0.22 ± 0.03
R_1 ($\Omega \text{ cm}^2$)	0.79 ± 0.07	0.70 ± 0.06	0.69 ± 0.06	0.97 ± 0.08	0.37 ± 0.05	0.38 ± 0.04	0.39 ± 0.06	0.46 ± 0.06
R_2 ($\Omega \text{ cm}^2$)	22.3 ± 0.9	18.7 ± 0.8	10.1 ± 0.6	4.55 ± 0.56	5.33 ± 0.68	5.12 ± 0.45	3.50 ± 0.46	1.88 ± 0.32
R_3 ($\Omega \text{ cm}^2$)	29.4 ± 1.1	15.1 ± 0.9	3.61 ± 0.45		2.29 ± 0.57	2.13 ± 0.52	0.70 ± 0.06	
Q_1 ($\text{m}\Omega^{-1} \text{ cm}^{-2} \text{ s}^b$)	57.6 ± 1.2	52.0 ± 0.7	45.2 ± 1.1	38.4 ± 0.8	77.7 ± 1.6	66.8 ± 1.2	44.5 ± 1.1	37.4 ± 1.3
n_1	0.56 ± 0.05	0.58 ± 0.04	0.58 ± 0.05	0.57 ± 0.07	0.58 ± 0.05	0.58 ± 0.04	0.60 ± 0.06	0.60 ± 0.04
Q_2 ($\text{m}\Omega^{-1} \text{ cm}^{-2} \text{ s}^b$)	35.9 ± 0.8	26.3 ± 1.0	21.9 ± 0.8	19.2 ± 0.9	37.6 ± 0.9	29.0 ± 0.8	23.2 ± 0.9	20.3 ± 0.7
n_2	0.91 ± 0.02	0.90 ± 0.04	0.89 ± 0.02	0.91 ± 0.06	0.89 ± 0.03	0.89 ± 0.12	0.87 ± 0.04	0.88 ± 0.03
C_p (mF cm^{-2})	13.7 ± 1.5	16.3 ± 2.3	15.8 ± 3.1		22.7 ± 2.2	24.7 ± 1.3	26.6 ± 3.0	
C_{dl} (mF cm^{-2})	26.4 ± 3.0	17.9 ± 1.6	13.5 ± 1.3	12.7 ± 1.4	23.7 ± 2.1	17.4 ± 1.4	12.0 ± 1.3	10.9 ± 0.46
R_f	1318	896	677	637	1186	872	599	547
Ni-AuNPs								
η (mV)	–20 mV	–65 mV	–110 mV	–150 mV	–20 mV	–65 mV	–110 mV	–150 mV
R_s ($\Omega \text{ cm}^2$)	0.59 ± 0.10	0.61 ± 0.08	0.59 ± 0.12	0.60 ± 0.09	0.46 ± 0.02	0.47 ± 0.01	0.47 ± 0.02	0.48 ± 0.03
R_1 ($\Omega \text{ cm}^2$)	0.17 ± 0.09	0.18 ± 0.08	0.22 ± 0.06	0.19 ± 0.05	0.09 ± 0.02	0.09 ± 0.04	0.11 ± 0.02	0.12 ± 0.03
R_2 ($\Omega \text{ cm}^2$)	2.06 ± 0.10	1.77 ± 0.12	1.23 ± 0.08	0.82 ± 0.09	0.52 ± 0.06	0.50 ± 0.07	0.46 ± 0.06	0.40 ± 0.05
Q_1 ($\text{m}\Omega^{-1} \text{ cm}^{-2} \text{ s}^b$)	151 ± 6	110 ± 7	90.7 ± 4.6	90.7 ± 6.5	165 ± 6.8	103 ± 5.2	95.0 ± 5.6	67.3 ± 4.8
n_1	0.58 ± 0.02	0.57 ± 0.02	0.57 ± 0.02	0.58 ± 0.02	0.63 ± 0.04	0.63 ± 0.04	0.64 ± 0.04	0.66 ± 0.05
Q_2 ($\text{m}\Omega^{-1} \text{ cm}^{-2} \text{ s}^b$)	40.9 ± 2.1	28.3 ± 1.6	20.1 ± 1.4	18.6 ± 1.6	42.3 ± 2.4	33.1 ± 1.8	28.4 ± 1.1	26.7 ± 1.2
n_2	0.91 ± 0.05	0.91 ± 0.03	0.93 ± 0.03	0.91 ± 0.06	0.91 ± 0.08	0.90 ± 0.06	0.91 ± 0.09	0.91 ± 0.04
C_{dl} (mF cm^{-2})	28.3 ± 2.1	18.5 ± 1.6	14.8 ± 1.4	11.7 ± 1.6	26.6 ± 2.4	19.6 ± 1.8	17.1 ± 1.1	16.0 ± 1.2
R_f	1417	926	740	584	1327	980	856	799

surface porosity [62, 63]. On the other hand, the diameter of the two overlapped semicircles observed in the range of medium to low frequencies decreases both with the overpotential and with the temperature. This fact indicates that both semicircles are connected to HER kinetics [62]. Both the C_{dl} and the R_2 decrease with cathodic overpotential; hence, the time constant associated with this semicircle is related to the HER charge transfer kinetics, namely to the response of double layer capacitance characterized by C_{dl} and the HER charge transfer resistance, R_2 . On the other hand, C_p remains almost constant with the cathodic overvoltage, while the value of R_3 decreases. This is a typical behavior related to the response of hydrogen adsorbed on an electrode surface, namely to the hydrogen adsorption capacitance, C_p , and resistance R_3 [31, 62, 68, 69].

As in the case of the porous Ni electrode, for the Ni-AuNPs, the high-frequency semicircle is almost constant with the overpotential and is related to the surface porosity [62, 63], while the low-frequency semicircle decreases with increasing the overpotential and the temperature is related to the kinetics of the HER. For the Ni-AuNPs electrode, the semicircle related to the adsorption relaxation apparently completely disappears. This is because the adsorption

process is facilitated by the AuNPs, and the charge transfer process dominates the impedance response as the potential increases. In fact, Watkins and Borensztein [70] have shown that although hydrogen cannot chemisorb at room temperature on extended gold surfaces, the dissociative adsorption of H_2 on AuNPs deposited on different oxides has been experimentally shown by different techniques.

For the two electrodes, the C_{dl} values decrease with the HER overpotential. This effect is attributed to an increasing formation of gas bubbles at higher overpotentials, which block the electrodes and, hence, are not electrochemically accessed by the electrolyte [71–74]. Furthermore, the C_{dl} decreases slowly with temperature. This effect can be explained due to the fact that at a same overpotential, the higher the temperature, the higher the apparent activity of the electrodes and, therefore, the current density. As a result, the hydrogen production increases, showing the same effect as that reported for the increase in the overpotential.

The value of C_{dl} was used to obtain the roughness factor (R_p), related to the effective surface area by a comparison with the value of for a smooth nickel electrode [68]. As can be observed in Fig. S4 (ESI) and in Table 2, for both electrodes, the roughness factor decreases with the increase

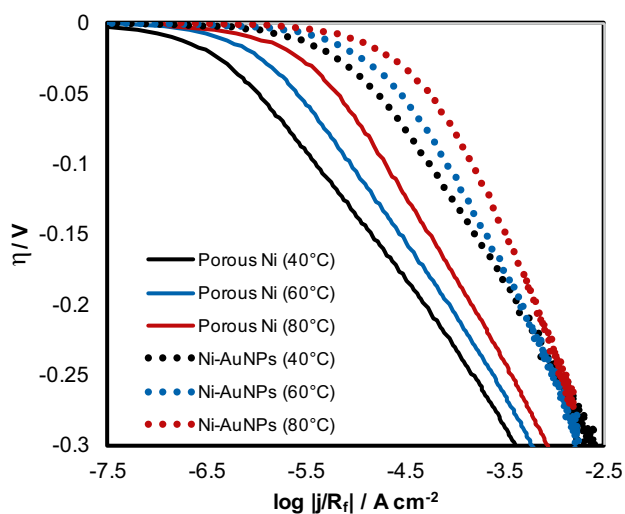


Fig. 9 Tafel representations of the investigated electrocatalysts corrected with R_f , recorded in 30 wt% KOH at different electrolyte temperatures

of overpotential and temperature. This decrease can be attributed to a blockage of a fraction of the inner surface of the electrode during HER due to gas bubbles shielding, hindering the access of the electrolyte [71, 73, 74]. The values of C_{dl} and R_f are slightly higher for Ni-AuNPs than for the porous Ni electrode, which indicates an increase in the active surface area. On the other hand, R_2 is considerably lower for Ni-AuNPs, indicating an improvement in the catalytic activity due to AuNPs. As for the Ni-AuNPs electrode, the real surface area is increased by approximately 20%; the lower resistance obtained with the Ni-AuNPs electrode can be attributed to an increase of the intrinsic catalytic activity due to AuNPs. In this way, it has been shown that the presence of AuNPs may improve the charge transport [75].

In order to remove the effect of the surface area, the Tafel representations were corrected with the values of R_f . This

Table 3 Kinetic parameters in the HER obtained from the correction of the Tafel representations with respect to the roughness factor, at different temperatures in 30 wt% KOH

Electrocatalyst	Temperature (°C)		
	40	60	80
Porous Ni			
b' (mV dec ⁻¹)	89	101	118
j_0/R_f ($\mu\text{A cm}^{-2}$)	0.29	0.90	2.92
α'	0.69	0.65	0.59
Ni-AuNPs			
b' (mV dec ⁻¹)	109	135	157
j_0/R_f ($\mu\text{A cm}^{-2}$)	6.59	15.4	35.2
α'	0.57	0.49	0.44

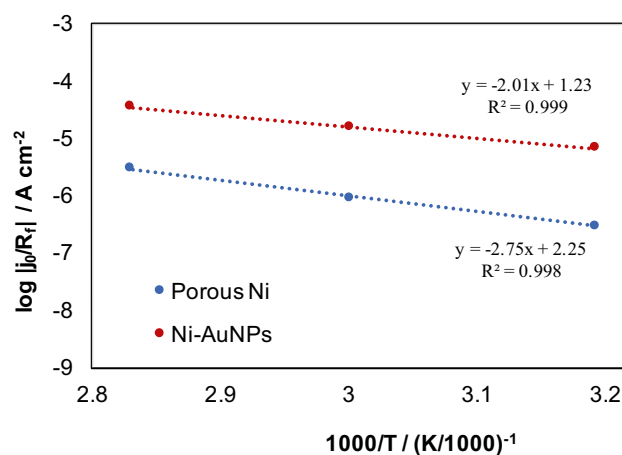


Fig. 10 Normalized Arrhenius representations of the investigated electrocatalysts in 30 wt% KOH

provides information about the intrinsic catalytic activity of the electrodes. As observed in Fig. 9, the catalytic effect of the AuNPs continues after removing the effect of the surface area. However, there exists an influence of the surface area, which can be observed by comparing the values of R_f and the distance between the curves in Figs. S2 (ESI) and 9.

The corrected kinetic parameters obtained from these representations are reported in Table 3. As can be observed, the corrected Tafel slopes (b') and charge transfer coefficients (α') of Ni-AuNPs are now closer to the values reported in the literature for a Volmer-Heyrovsky mechanism in the HER [27, 53]. Likewise, the corrected values of the exchange current density (j_0/R_f) are represented logarithmically in Fig. 10 vs the inverse of temperature to obtain the new Arrhenius representations and, therefore, normalized values of the activation energies (E_a'), which are listed in Table 4. After removing the effect of the surface area, the activation energy remains almost constant.

From the results obtained from the Tafel representations and the EIS study, it is derived that, for the Ni porous electrode, the semicircle associated to the response of hydrogen adsorbed on the electrode surface (C_p and R_3), decreases faster with the overpotential than the semicircle associated to the charge transfer process (CPE_2 and R_2), and for the Ni-AuNPs electrode, the semicircle associated to the response of hydrogen adsorbed disappears. This is due to the fact that the adsorption process is facilitated and the charge transfer process dominates the impedance response as the potential increases. On the other hand, the values found for the free

Table 4 Corrected activation energies of the electrocatalysts obtained in 30 wt% KOH

Electrocatalyst	E_a' (kJ mol ⁻¹)
Porous Ni	52.7 ± 0.1
Ni-AuNPs	38.5 ± 0.1

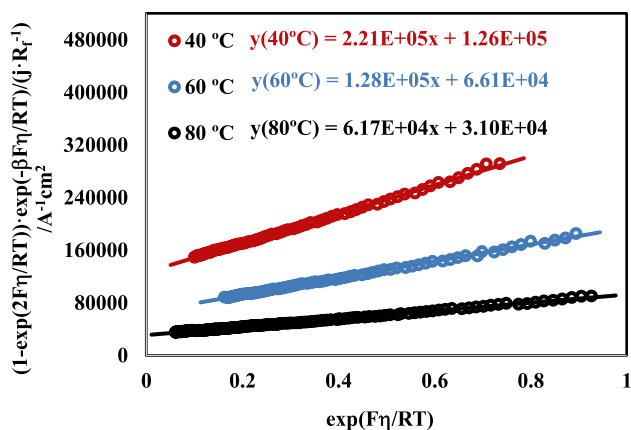


Fig. 11 Testing of the Volmer-Heyrovsky mechanism for the HER on the electrode modified with AuNPs at 40, 60, and 80 °C in 30 wt% KOH

activation energy are very close to those usually postulated for the HER occurring through the Volmer-Heyrovsky mechanism on Ni surfaces [60, 61].

According to Lasia [75], and considering no mass transfer limitations and equal symmetry factor for the Volmer and Heyrovsky reactions, the current density can be expressed as:

$$j = \frac{2Fk_1k_2e^{-\frac{\beta F\eta}{RT}} \left(1 - e^{\frac{2F\eta}{RT}}\right)}{(k_1+k_2) + (k_{-1}+k_{-2})e^{\frac{F\eta}{RT}}} \quad (7)$$

where k_1 and k_{-1} are the Volmer rate constants, k_2 and k_{-2} are the Heyrovsky rate constants, and β is the symmetry factor and equals the charge transfer coefficient. Equation (7) may produce two Tafel slopes [75]. This equation can be linearized as:

$$\frac{e^{-\frac{\beta F\eta}{RT}} \left(1 - e^{\frac{2F\eta}{RT}}\right)}{j} = \frac{1}{j_h^0} + \frac{1}{j_l^0} e^{\frac{F\eta}{RT}} \quad (8)$$

where j_h^0 is the exchange current density extrapolated from the Tafel representations of the corrected current density $j/1 - e^{\frac{2F\eta}{RT}}$ at low overpotentials and j_l^0 is the exchange current density extrapolated from the Tafel representations of the corrected current density at high overpotentials, and they are related to the rate constants as:

$$j_h^0 = \frac{2F}{\frac{1}{k_1} + \frac{1}{k_2}} \quad (9)$$

$$j_l^0 = \frac{2F}{\frac{1}{k_{-1}} + \frac{1}{k_{-2}}} \quad (10)$$

Table 5 Exchange current densities for the electrode modified with AuNPs in 30 wt% KOH

Temperature (°C)	j_h^0 (μAcm^{-2})	j_l^0/R_s ($\mu\text{A cm}^{-2}$)
40	7.90	6.59
60	15.1	15.4
80	32.2	35.2

If the HER takes place by the Volmer-Heyrovsky mechanism and only one Tafel slope is observed, θ_H is constant, the rates of the Volmer and Heyrovsky steps are identical, and a

representation of $\frac{e^{-\frac{\beta F\eta}{RT}} \left(1 - e^{\frac{2F\eta}{RT}}\right)}{j}$ vs $e^{\frac{F\eta}{RT}}$ should result in a straight line with similar values of slope and intercept. This is shown in Fig. 11 at 40, 60, and 80 °C, where a good linearity can be observed. This representation has been obtained assuming that the symmetry factor equals the charge transfer coefficient shown in Table 3. In this case, and considering Eq. (9), Eq. (7) can be simplified to Eq. (11).

$$j = j_h^0 e^{-\frac{\beta F\eta}{RT}} \quad (11)$$

The values of j_h^0 are similar to the values obtained from the Tafel representations (Table 5). This confirms the assumption about the mechanism of the HER.

From these results, it is evident that the AuNPs significantly improve the catalytic performance of the electrode mainly due to their intrinsic activity, and there is only a slight influence of the increase in the surface area. AuNPs incorporated on a porous Ni electrode by heat treatment were previously reported with very good results in the HER [19]; however, in this work, the modification of the Ni electrode with the gold nanoparticles was easier and effective; the particles remain in the electrode after the electrochemical characterization.

Conclusions

Well-dispersed Au nanoparticles were successfully synthesized by chemical reduction using NaBH_4 as reducing agent and PVP as stabilizing agent. The nanoparticles were easily incorporated by heat treatment, onto the surface of a porous Ni electrode fabricated by electrodeposition at a high current density. The size of the nanoparticles remains nearly the same after the heat treatment, and agglomeration was largely avoided thanks to the PVP coverage of the nanoparticles. The effect of the nanoparticles in the HER was studied by pseudo-steady-state polarization curves and EIS and compared with a pure porous Ni electrode at different temperatures.

The addition of the AuNPs clearly improved the catalytic performance of the electrode mainly due to their intrinsic catalytic activity and, at some extent, by the increase of the active surface area, which was concluded by the study of the real surface area provided by the EIS. The HER takes place by the Volmer-Heyrovsky mechanism.

Supplementary Information The online version contains supplementary material available at <https://doi.org/10.1007/s12678-021-00690-7>.

Acknowledgements Ramiro Medina Orta is grateful to Consejo Nacional Ciencia y Tecnología and Consejo Potosino de Ciencia y Tecnología for the doctorate scholarship 472041. Also, he wishes to thank the Instituto de Metalurgia of Universidad Autónoma de San Luis Potosí for the opportunity of a research stay. We also thank Dr. Nubia Arteaga Larios and M.M.I.M. Martha Alejandra Lomelí Pacheco (Instituto de Metalurgia, Universidad Autónoma de San Luis Potosí) for their help with the UV-vis spectroscopy.

References

- M.A. El-Sayed, Some interesting properties of metals confined in time and nanometer space of different shapes. *Acc. Chem. Res.* **34**, 257–264 (2001)
- E. Roduner, Size matters: why nanomaterials are different. *Chem. Soc. Rev.* **35**, 583–592 (2006). <https://doi.org/10.1039/b502142c>
- J. Belloni, Metal nanocolloids. *Curr. Opin. Colloid Interface Sci.* **1**, 184–196 (1996). [https://doi.org/10.1016/S1359-0294\(96\)80003-3](https://doi.org/10.1016/S1359-0294(96)80003-3)
- R. Narayanan, M.A. El-Sayed, Catalysis with transition metal nanoparticles in colloidal solution: nanoparticle shape dependence and stability. *J. Phys. Chem. B.* **109**, 12663–12676 (2005)
- F. Pagnanelli, P. Altimari, M. Bellagamba, G. Granata, E. Moscardini, P.G. Schiavi, L. Toro, Pulsed electrodeposition of cobalt nanoparticles on copper: influence of the operating parameters on size distribution and morphology. *Electrochim. Acta.* **155**, 228–235 (2015). <https://doi.org/10.1016/j.electacta.2014.12.112>
- Q. Wang, J. Zheng, Electrodeposition of silver nanoparticles on a zinc oxide film: Improvement of amperometric sensing sensitivity and stability for hydrogen peroxide determination. *Microchim. Acta.* **169**, 361–365 (2010). <https://doi.org/10.1007/s00604-010-0356-7>
- L. Rodríguez-Sánchez, M.C. Blanco, M.A. López-Quintela, Electrochemical synthesis of silver nanoparticles. *J. Phys. Chem. B.* **104**, 9683–9688 (2000). <https://doi.org/10.1021/jp001761r>
- P.M. Uberman, L.A. Pérez, G.I. Lacconi, S.E. Martín, PVP-stabilized palladium nanoparticles electrochemically obtained as effective catalysts in aqueous medium Suzuki-Miyaura reaction. *J. Mol. Catal. A Chem.* **363–364**, 245–253 (2012). <https://doi.org/10.1016/j.molcata.2012.06.016>
- W. Pan, X. Zhang, H. Ma, J. Zhang, Electrochemical synthesis, voltammetric behavior, and electrocatalytic activity of Pd nanoparticles. *J. Phys. Chem. C.* **112**, 2456–2461 (2008). <https://doi.org/10.1021/jp710092z>
- B. Yin, H. Ma, S. Wang, S. Chen, Electrochemical synthesis of silver nanoparticles under protection of poly(n-vinylpyrrolidone). *J. Phys. Chem. B.* **107**, 8898–8904 (2003). <https://doi.org/10.1021/jp0349031>
- K.B. Narayanan, N. Sakthivel, Synthesis and characterization of nano-gold composite using *Cylindrocladium floridanum* and its heterogeneous catalysis in the degradation of 4-nitrophenol. *J. Hazard. Mater.* **189**, 519–525 (2011). <https://doi.org/10.1016/j.jhazmat.2011.02.069>
- H. Veisi, S. Azizi, P. Mohammadi, Green synthesis of the silver nanoparticles mediated by *Thymra spicata* extract and its application as a heterogeneous and recyclable nanocatalyst for catalytic reduction of a variety of dyes in water. *J. Clean. Prod.* **170**, 1536–1543 (2018). <https://doi.org/10.1016/j.jclepro.2017.09.265>
- Y. Wang, D. O'Connor, Z. Shen, I.M.C. Lo, D.C.W. Tsang, S. Pehkonen, S. Pu, D. Hou, Green synthesis of nanoparticles for the remediation of contaminated waters and soils: constituents, synthesizing methods, and influencing factors. *J. Clean. Prod.* **226**, 540–549 (2019). <https://doi.org/10.1016/j.jclepro.2019.04.128>
- M. Teimouri, F. Khosravi-Nejad, F. Attar, A.A. Saboury, I. Kostova, G. Benelli, M. Falahati, Gold nanoparticles fabrication by plant extracts: synthesis, characterization, degradation of 4-nitrophenol from industrial wastewater, and insecticidal activity – a review. *J. Clean. Prod.* **184**, 740–753 (2018). <https://doi.org/10.1016/j.jclepro.2018.02.268>
- I. Pedre, F. Battaglini, G.J. Labrada-Delgado, M.G. Sánchez-Loredo, G.A. González, Detection of thiourea from electrorefining baths using silver nanoparticles-based sensors, sensors actuators. *B Chem.* **211**, 515–522 (2015). <https://doi.org/10.1016/j.snb.2015.01.074>
- N.R. Jana, Z.L. Wang, T. Pal, Redox catalytic properties of palladium nanoparticles: surfactant and electron donor-acceptor effects. *Langmuir* **16**, 2457–2463 (2000). <https://doi.org/10.1021/la990507r>
- R. Fenger, E. Fertitta, H. Kirmse, A.F. Thünemann, K. Rademann, Size dependent catalysis with CTAB-stabilized gold nanoparticles. *Phys. Chem. Chem. Phys.* **14**, 9343–9349 (2012). <https://doi.org/10.1039/c2cp40792b>
- C. Huff, T. Dushatinski, T.M. Abdel-Fattah, Gold nanoparticle/multi-walled carbon nanotube composite as novel catalyst for hydrogen evolution reactions. *Int. J. Hydrogen Energy.* **42**, 18985–18990 (2017). <https://doi.org/10.1016/j.ijhydene.2017.05.226>
- C. González-Buch, I. Herraiz-Cardona, E.M. Ortega, S. Mestre, V. Pérez-Herranz, Synthesis and characterization of Au-modified macroporous Ni electrocatalysts for alkaline water electrolysis. *Int. J. Hydrogen Energy.* **41**, 764–772 (2016). <https://doi.org/10.1016/j.ijhydene.2015.10.142>
- M.A. Amin, S.A. Fadlallah, G.S. Alosaimi, In situ aqueous synthesis of silver nanoparticles supported on titanium as active electrocatalyst for the hydrogen evolution reaction. *Int. J. Hydrogen Energy.* **39**, 19519–19540 (2014). <https://doi.org/10.1016/j.ijhydene.2014.09.100>
- M.A. Amin, S.A. Fadlallah, G.S. Alosaimi, F. Kandemirli, M. Saracoglu, S. Szunerits, R. Boukherroub, Cathodic activation of titanium-supported gold nanoparticles: an efficient and stable electrocatalyst for the hydrogen evolution reaction. *Int. J. Hydrogen Energy.* **41**, 6326–6341 (2016). <https://doi.org/10.1016/j.ijhydene.2016.02.107>
- V. Pérez-Herranz, R. Medina, P. Taymans, C. González-Buch, E.M. Ortega, G. Sánchez-Loredo, G.J. Labrada-Delgado, Modification of porous nickel electrodes with silver nanoparticles for hydrogen production. *J. Electroanal. Chem.* **808**, 420–426 (2018). <https://doi.org/10.1016/j.jelechem.2017.06.022>
- T.N. Veziroğlu, S. Şahin, 21st century's energy: hydrogen energy system. *Energy Convers. Manag.* **49**, 1820–1831 (2008). <https://doi.org/10.1016/j.enconman.2007.08.015>
- K. Mazloomi, C. Gomes, Hydrogen as an energy carrier: prospects and challenges. *Renew. Sustain. Energy Rev.* **16**, 3024–3033 (2012). <https://doi.org/10.1016/j.rser.2012.02.028>
- J.O.M. Bockris, T.N. Veziroğlu, A solar-hydrogen economy for U.S.A., *Int. J. Hydrogen Energy.* **8**, 323–340 (1983). [https://doi.org/10.1016/0360-3199\(83\)90048-4](https://doi.org/10.1016/0360-3199(83)90048-4).

26. F. Barbir, Transition to renewable energy systems with hydrogen as an energy carrier. *Energy* **34**, 308–312 (2009). <https://doi.org/10.1016/j.energy.2008.07.007>
27. A. Lasia, A. Rami, Kinetics of hydrogen evolution on nickel electrodes. *J. Electroanal. Chem.* **294**, 123–141 (1990). [https://doi.org/10.1016/0022-0728\(90\)87140-F](https://doi.org/10.1016/0022-0728(90)87140-F)
28. Y. Choquette, L. Brossard, A. Lasia, H. Ménard, Investigation Raney-nickel electrodes. *Electrochim. Acta.* **35**, 1251–1256 (1990)
29. R. Solmaz, A. Döner, G. Kardaş, The stability of hydrogen evolution activity and corrosion behavior of NiCu coatings with long-term electrolysis in alkaline solution. *Int. J. Hydrogen Energy.* **34**, 2089–2094 (2009). <https://doi.org/10.1016/j.ijhydene.2009.01.007>
30. I. Arul-Raj, V.K. Venkatesan, Characterization of nickel-molybdenum and nickel-molybdenum-iron alloy coatings as cathodes for alkaline water electrolyzers. *Int. J. Hydrogen Energy.* **13**, 215–223 (1988). [https://doi.org/10.1016/0360-3199\(88\)90088-2](https://doi.org/10.1016/0360-3199(88)90088-2)
31. E. Navarro-Flores, Z. Chong, S. Omanovic, Characterization of Ni, NiMo, NiW and NiFe electroactive coatings as electrocatalysts for hydrogen evolution in an acidic medium. *J. Mol. Catal. A Chem.* **226**, 179–197 (2005). <https://doi.org/10.1016/j.molcata.2004.10.029>
32. I. Herraiz-Cardona, E.M. Ortega, L. Vázquez-Gómez, V. Pérez-Herranz, Electrochemical characterization of a NiCo/Zn cathode for hydrogen generation. *Int. J. Hydrogen Energy.* **36**, 11578–11587 (2011). <https://doi.org/10.1016/j.ijhydene.2011.06.067>
33. I. Herraiz-Cardona, E.M. Ortega, L. Vázquez-Gómez, V. Pérez-Herranz, Double-template fabrication of three-dimensional porous nickel electrodes for hydrogen evolution reaction. *Int. J. Hydrogen Energy.* **37**, 2147–2156 (2012). <https://doi.org/10.1016/j.ijhydene.2011.09.155>
34. C. González-Buch, I. Herraiz-Cardona, E.M. Ortega, J. García-Antón, V. Pérez-Herranz, Synthesis and characterization of macroporous Ni, Co and Ni-Co electrocatalytic deposits for hydrogen evolution reaction in alkaline media. *Int. J. Hydrogen Energy.* **38**, 10157–10169 (2013). <https://doi.org/10.1016/j.ijhydene.2013.06.016>
35. J. Kim, S. Byun, A.J. Smith, J. Yu, J. Huang, Enhanced electrocatalytic properties of transition-metal dichalcogenides sheets by spontaneous gold nanoparticle decoration. *J. Phys. Chem. Lett.* **4**, 1227–1232 (2013). <https://doi.org/10.1021/jz400507t>
36. D. Li, J. Lao, C. Jiang, C. Luo, R. Qi, H. Lin, R. Huang, G.I.N. Waterhouse, H. Peng, Plasmonic Au nanoparticle-decorated Bi₂Se₃ nanoflowers with outstanding electrocatalytic performance for hydrogen evolution. *Int. J. Hydrogen Energy.* **44**, 30876–30884 (2019). <https://doi.org/10.1016/j.ijhydene.2019.10.041>
37. D. Balun-Kayan, D. Koçak, M. İlhan, Electrocatalytic hydrogen production on GCE/RGO/Au hybrid electrode. *Int. J. Hydrogen Energy.* **43**, 10562–10568 (2018). <https://doi.org/10.1016/j.ijhydene.2018.01.077>
38. Y. Pan, M. Wen, Noble metals enhanced catalytic activity of anatase TiO₂ for hydrogen evolution reaction. *Int. J. Hydrogen Energy.* **43**, 22055–22063 (2018). <https://doi.org/10.1016/j.ijhydene.2018.10.093>
39. C. González-Buch, I. Herraiz-Cardona, E.M. Ortega, J. García-Antón, V. Pérez-Herranz, Study of the catalytic activity of 3D macroporous Ni and NiMo cathodes for hydrogen production by alkaline water electrolysis. *J. Appl. Electrochem.* **46**, 791–803 (2016). <https://doi.org/10.1007/s10800-016-0970-0>
40. R.S. Sai Siddhardha, V. Lakshminarayanan, S.S. Ramamurthy, Spot-free catalysis using gold carbon nanotube & gold graphene composites for hydrogen evolution reaction, *J. Power Sources.* **288**, 441–450 (2015). <https://doi.org/10.1016/j.jpowsour.2015.04.141>
41. G. Mie, Beiträge zur Optik trüber Medien, speziell kolloidaler Metallösungen. *Ann. Der Physic.* **330**, 377–445 (1908). <https://doi.org/10.1002/andp.19083300302>
42. K.M. Koczkur, S. Mourdikoudis, L. Polavarapu, S.E. Skrabalak, Polyvinylpyrrolidone (PVP) in nanoparticle synthesis. *Dalt. Trans.* **44**, 17883–17905 (2015). <https://doi.org/10.1039/c5dt02964c>
43. R. Si, Y.W. Zhang, L.P. You, C.H. Yan, Self-organized monolayer of nanosized ceria colloids stabilized by poly(vinylpyrrolidone). *J. Phys. Chem. B.* **110**, 5994–6000 (2006). <https://doi.org/10.1021/jp057501x>
44. Y. Gao, P. Jiang, D.F. Liu, H.J. Yuan, X.Q. Yan, Z.P. Zhou, J.X. Wang, L. Song, L.F. Liu, W.Y. Zhou, G. Wang, C.Y. Wang, S.S. Xie, J.M. Zhang, D.Y. Shen, Evidence for the monolayer assembly of poly(vinylpyrrolidone) on the surfaces of silver nanowires. *J. Phys. Chem. B.* **108**, 12877–12881 (2004). <https://doi.org/10.1021/jp037116c>
45. X.L. Tang, P. Jiang, G.L. Ge, M. Tsuji, S.S. Xie, Y.J. Guo, Poly(N-vinyl-2-pyrrolidone) (PVP)-capped dendritic gold nanoparticles by a one-step hydrothermal route and their high SERS effect. *Langmuir* **24**, 1763–1768 (2008). <https://doi.org/10.1021/la703495s>
46. H.H. Huang, X.P. Ni, G.L. Loy, C.H. Chew, K.L. Tan, F.C. Loh, J.F. Deng, G.Q. Xu, Photochemical formation of silver nanoparticles in poly(N-vinylpyrrolidone). *Langmuir* **12**, 909–912 (1996). <https://doi.org/10.1021/la950435d>
47. F. Bonet, K. Tekaiia-Elhssissen, K. Vijaya-Sarathy, Study of interaction of ethylene glycol/PVP phase on noble metal powders prepared by polyol process. *Bull. Mater. Sci.* **23**, 165–168 (2000). <https://doi.org/10.1007/BF02719903>
48. G. Carotenuto, G.P. Pepe, L. Nicolais, Preparation and characterization of nano-sized Ag / PVP. *Eur. Phys. J. B.* **16**, 11–17 (2000)
49. G. Carotenuto, S. DeNicola, G.P. Pepe, L. Nicolais, A qualitative model for the growth mechanism of silver clusters in polymer solution. *Eur. Phys. J. B.* **24**, 437–441 (2001). <https://doi.org/10.1007/s10051-001-8696-z>
50. Z. Chen, J.W. Chang, C. Balasanthiran, S.T. Milner, R.M. Rioux, Anisotropic growth of silver nanoparticles is kinetically controlled by polyvinylpyrrolidone binding. *J. Am. Chem. Soc.* **141**, 4328–4337 (2019). <https://doi.org/10.1021/jacs.8b11295>
51. C. Chen, D.Y.W. Ng, T. Weil, Polymer-grafted gold nanoflowers with temperature-controlled catalytic features by: in situ particle growth and polymerization. *Mater. Chem. Front.* **3**, 1449–1453 (2019). <https://doi.org/10.1039/c9qm00252a>
52. M.F. Kibria, M.S. Mridha, A.H. Khan, Electrochemical studies of a nickel electrode for the hydrogen evolution reaction. *Int. J. Hydrogen Energy.* **20**, 435–440 (1995). [https://doi.org/10.1016/0360-3199\(94\)00073-9](https://doi.org/10.1016/0360-3199(94)00073-9)
53. A. Rami, A. Lasia, Kinetics of hydrogen evolution on Ni-Al alloy electrodes. *J. Appl. Electrochem.* **22**, 376 (1992). <https://doi.org/10.1007/BF01092692>
54. L.A. Khanova, L.I. Krishtalik, Kinetics of the hydrogen evolution reaction on gold electrode. A new case of the barrierless discharge, *J. Electroanal. Chem.* **660**, 224–229 (2011). <https://doi.org/10.1016/j.jelechem.2011.01.016>
55. T. Ohmori, M. Enyo, Hydrogen evolution reaction on gold electrode in alkaline solutions. *Electrochim. Acta.* **37**, 2021–2028 (1992). [https://doi.org/10.1016/0013-4686\(92\)87118-J](https://doi.org/10.1016/0013-4686(92)87118-J)
56. A. Kahyarian, B. Brown, S. Nestic, Mechanism of the hydrogen evolution reaction in mildly acidic environments on gold. *J. Electrochem. Soc.* **164**, H365–H374 (2017). <https://doi.org/10.1149/2.1061706jes>
57. A. Lasia, Hydrogen evolution reaction, in: *Handb. Fuel Cells*, John Wiley & Sons, Ltd, Chichester, UK, (2010). <https://doi.org/10.1002/9780470974001.f204033>
58. A.N. Correia, S.A.S. Machado, Hydrogen evolution on electrodeposited Ni and Hg ultramicroelectrodes. *Electrochim. Acta.* **43**, 367–373 (1998). [https://doi.org/10.1016/S0013-4686\(97\)00050-9](https://doi.org/10.1016/S0013-4686(97)00050-9)
59. O. Savadogo, E. Ndzebet, Influence of SiW₁₂O₄₀⁴⁻ on the electrocatalytic behaviour of Pt-Co alloy supported on carbon for

- water electrolysis in 3 M KOH aqueous solution. *Int. J. Hydrogen Energy*. **26**, 213–218 (2001). [https://doi.org/10.1016/S0360-3199\(00\)00059-8](https://doi.org/10.1016/S0360-3199(00)00059-8)
60. S.A.S. Machado, L.A. Avaca, The hydrogen evolution reaction on nickel surfaces stabilized by H-absorption. *Electrochim. Acta*. **39**, 1385–1391 (1994). [https://doi.org/10.1016/0013-4686\(94\)E0003-1](https://doi.org/10.1016/0013-4686(94)E0003-1)
61. B.E. Conway, L. Bai, H₂ evolution kinetics at high activity Ni-Mo-Cd electrocoated cathodes and its relation to potential dependence of sorption of H. *Int. J. Hydrogen Energy*. **11**, 533–540 (1986). [https://doi.org/10.1016/0360-3199\(86\)90020-0](https://doi.org/10.1016/0360-3199(86)90020-0)
62. L. Birry, A. Lasia, Studies of the hydrogen evolution reaction on Raney nickel-molybdenum electrodes. *J. Appl. Electrochem.* **34**, 735–749 (2004)
63. C. Hitz, A. Lasia, Experimental study and modeling of impedance of porous electrodes. *J. Electroanal. Chem.* **500**, 213–222 (2001)
64. R. de Levie, in P. Delahay (Ed.), *Advances in electrochemistry and electrochemical engineering*. Interscience, New York, **6**, 329 (1967).
65. L. Chen, A. Lasia, Study of the kinetics of hydrogen evolution reaction on nickel-zinc powder electrodes. *J. Electrochem. Soc.* **139**, 3214–3219 (1992). <https://doi.org/10.1149/1.2069055>
66. R.D. Armstrong, M. Henderson, Impedance plane display of a reaction with an adsorbed intermediate, *Electroanal. Chem. Interfacial. Electrochem.* **39**, 81–90 (1972)
67. G.J. Brug, a. L.G. van den Eeden, M. Sluyters-Rehbach, J.H. Sluyters, The analysis of electrode impedances complicated by the presence of a constant phase element. *J. Electroanal. Chem.* **176**, 275–295 (1984). [https://doi.org/10.1016/S0022-0728\(84\)80324-1](https://doi.org/10.1016/S0022-0728(84)80324-1)
68. I. Herraiz-Cardona, E.M. Ortega, J. García-Antón, V. Pérez-Herranz, Assessment of the roughness factor effect and the intrinsic catalytic activity for hydrogen evolution reaction on Ni-based electrodeposits. *Int. J. Hydrogen Energy*. **36**, 9428–9438 (2011). <https://doi.org/10.1016/j.ijhydene.2011.05.047>
69. I. Herraiz-Cardona, E. Ortega, V. Pérez-Herranz, Impedance study of hydrogen evolution on Ni/Zn and Ni-Co/Zn stainless steel based electrodeposits. *Electrochim. Acta*. **56**, 1308–1315 (2011). <https://doi.org/10.1016/j.electacta.2010.10.093>
70. W.L. Watkins, Y. Borensztein, Mechanism of hydrogen adsorption on gold nanoparticles and charge transfer probed by anisotropic surface plasmon resonance. *Phys. Chem. Chem. Phys.* **19**, 27397–27405 (2017). <https://doi.org/10.1039/c7cp04843b>
71. V. Ganesh, V. Lakshminarayanan, Preparation of high surface area nickel electrodeposit using a liquid crystal template technique. *Electrochim. Acta*. **49**, 3561–3572 (2004). <https://doi.org/10.1016/j.electacta.2004.03.024>
72. S. Rausch, H. Wendt, Morphology and Utilization of smooth hydrogen-evolving Raney nickel cathode coatings and porous sintered-nickel cathodes. *J. Electrochem. Soc.* **143**, 2852–2862 (1996). <https://doi.org/10.1149/1.1837118>
73. A. Kellenberger, N. Vaszilcsin, W. Brandl, N. Duteanu, Kinetics of hydrogen evolution reaction on skeleton nickel and nickel-titanium electrodes obtained by thermal arc spraying technique. *Int. J. Hydrogen Energy*. **32**, 3258–3265 (2007). <https://doi.org/10.1016/j.ijhydene.2007.02.028>
74. B. Pierozynski, L. Smoczynski, Kinetics of hydrogen evolution reaction at nickel-coated carbon fiber materials in 0.5 M H₂SO₄ and 0.1 M NaOH solutions. *J. Electrochem. Soc.* **156**, B1045 (2009). <https://doi.org/10.1149/1.3158518>
75. A. Lasia, Mechanism and kinetics of the hydrogen evolution reaction. *Int. J. Hydrogen Energy* **44**, 19484–19518 (2019)

Publisher's Note Springer Nature remains neutral with regard to jurisdictional claims in published maps and institutional affiliations.